Six-degree-of-freedom magnetic actuation for wireless microrobotics

Eric Diller[1], Joshua Giltinan[2], Guo Zhan Lum[2], Zhou Ye[2] and Metin Sitti[2,3]

Abstract

Existing remotely actuated magnetic microrobots exhibit a maximum of only five-degree-of-freedom (DOF) actuation, as creation of a driving torque about the microrobot magnetization axis is not achievable. This lack of full orientation control limits the effectiveness of existing microrobots for precision tasks of object manipulation and orientation for advanced medical, biological and micromanufacturing applications. This paper presents a magnetic actuation method that allows remotely powered microrobots to achieve full six-DOF actuation by considering the case of a non-uniform magnetization profile within the microrobot body. This non-uniform magnetization allows for additional rigid-body torques to be induced from magnetic forces via a moment arm. A general analytical model presents the working principle for continuous and discrete magnetization profiles, which is applied to permanent or non-permanent (soft) magnet bodies. Several discrete-magnetization designs are also presented which possess reduced coupling between magnetic forces and induced rigid-body torques. Design guidelines are introduced which can be followed to ensure that a magnetic microrobot design is capable of six-DOF actuation. A simple permanent-magnet prototype is fabricated and used to quantitatively demonstrate the accuracy of the analytical model in a constrained-DOF environment and qualitatively for free motion in a viscous liquid three-dimensional environment. Results show that desired forces and torques can be created with high precision and limited parasitic actuation, allowing for full six-DOF actuation using limited feedback control.

Keywords

Microrobots, six-DOF, magnetic actuation

1. Introduction

Remote magnetic actuation provides advantages over other mobile microrobot actuation methods in its ability to apply relatively large forces and torques at a distance. It also allows for penetration through most materials, including biological materials for potential applications in microfluidics (Ye et al., 2012; Ye and Sitti, 2014), microfactories (Khamesee et al., 2002; Elbuken et al., 2009; Diller and Sitti, 2014), bioengineering (Kim et al., 2013; Tasoglu et al., 2014; Chung et al., 2015), and healthcare (Martel et al., 2007; Frutiger et al., 2009; Martel et al., 2009; Kummer et al., 2010; Sakar et al., 2011; Diller et al., 2012; Mahoney et al., 2012; Tottori et al., 2012; Vartholomeos et al., 2012; Diller et al., 2013a; Diller and Sitti, 2013; Khalil et al., 2014; Vartholomeos et al., 2013; Diller et al., 2014b). However, magnetic actuation of permanent or non-permanent (soft) magnets operating far from the driving coils have been limited to only five-degree-of-freedom (DOF) actuation, while other actuation methods often have even fewer available DOFs. In particular, previous magnetic actuation schemes have not been able to apply

magnetic torque about the magnet's magnetization axis. The limitation prevents a robotic element from directly assuming any desired orientation in its workspace. As microrobots and their applications become more complex, this actuation limitation is increasingly hindering their motion and manipulation dexterity.

To accommodate a lack of full six-DOF control, current magnetic microrobots have often been designed to be geometrically symmetric about their magnetization axis. Such axisymmetric designs can eliminate the need for rotation control about a single axis. For example, axisymmetric magnetic microrobots have been demonstrated to puncture blood vessels with a cylindrical syringe (Kummer et al.,

[1]University of Toronto, Toronto, ON, Canada
[2]Carnegie Mellon University, Pittsburgh, PA, USA
[3]Max Planck Institute for Intelligent Systems, Stuttgart, Germany

Corresponding author:
Metin Sitti, Max Planck Institute for Intelligent Systems, Heisenbergstr. 3, 70569 Stuttgart, Germany.
Email: sitti@cmu.edu, sitti@is.mpg.de

2010) and non-contact manipulators used spherical symmetry to create predicted Stokes flows (Ye et al., 2012). However, as microrobots become available for more advanced applications (Pawashe et al., 2012; Diller et al., 2013b; Miyashita et al., 2013), the demands on their functionality have been increasing. Microrobots for advanced manipulation and mobility applications will be required to achieve all six-DOF dexterity similar to that achieved by large-scale robotic manipulators. Centimeter-scale magnetic devices have achieved six-DOF motion by actuating multiple discrete magnets with non-uniform magnetic fields (Miyasaka and Berkelman, 2014). However, the underlying theory of magnetic microrobots often assumes the magnetic field is uniform in the microrobot workspace. Thus, this principle cannot be applied to microrobots in a uniform workspace.

We present here a magnetic actuation method which is able to overcome the challenge seen by previous magnetic actuation schemes to enable six-DOF magnetic actuation using driving coils far from the workspace. While previous studies in magnetic microrobot actuation assume uniform magnetization throughout the magnetic volume of the microrobot, we relax this assumption here. By allowing for varying magnetization in the volume of the magnet, additional coupling is encountered between applied magnetic forces and their induced rigid-body torques. This allows for the creation of rigid-body torques about any axis, without loss of actuation force command.

A preliminary version of this work was presented as a conference paper (Diller et al., 2014a), where the concept for six-DOF magnetic actuation was introduced with experimental verification. This work expands on that paper through two areas of new content. The first is in the introduction of a set of design guidelines based on the necessary conditions which a microrobot designer can use to ensure that their design will allow for actuation in all six DOFs. The second significant addition is an extension of the actuation technique to non-permanent (soft) magnet designs.

In this paper, we first formulate in Section 2 the six-DOF actuation concept for a general magnetic body with distributed arbitrary magnetization profile and the proposed design methodologies, and then discuss in Section 3 the case of multiple discrete magnetic elements, each with uniform magnetization. For the discrete case, we show that several magnet arrangements are possible which reduce the coupling between magnetic forces and torques and their corresponding rigid body forces and torques. These decoupling arrangements allow for a simpler description of the actuation. We also show solutions for non-permanent magnets. Section 4 introduces control methods for open-loop and closed-loop actuation of six-DOF microrobots. In Section 5, we experimentally validate the analytical model through reduced-DOF water surface experiments and demonstrate full six-DOF motion in a liquid environment for permanent-magnet microrobot designs. The paper is concluded in Section 6.
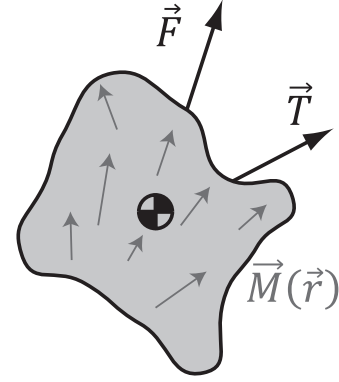

Fig. 1. Schematic of a general magnet with distributed magnetization profile, showing the magnetic force and torque exerted on the rigid body.

2. Concept

2.1. Magnetic force and torque

Magnetic forces and torques are assumed to be applied to actuate a microrobot using fields applied from magnetic coils outside the operating workspace. It is also assumed that the fields and their spatial gradients in the workspace can be generated independently while obeying Gauss's and Ampere's laws. A general magnet with spatially distributed non-uniform magnetization profile $\vec{M} = \vec{M}(\vec{r}, \vec{B})$ is shown in Figure 1. Here, $\vec{r}$ denotes the position of a point within the magnet relative to the magnet center of mass (COM). The results in this section are valid for permanent or non-permanent (soft) magnet bodies, but for brevity we will not continue to indicate the magnetization profile's explicit dependence on the applied field $\vec{B}$, but rather assume that a knowledge of $\vec{M}$ is known as the starting point in this analysis. The net magnetic moment quantity $\vec{m}_e$ is found by integrating the magnetization over the volume as $\vec{m}_e = \int M dV$. The magnetic force distribution $\vec{f}(\vec{r})$ exerted on a microrobot over the volume V in a magnetic field $\vec{B}$, assuming no electric current is flowing in the volume being integrated, is integrated to give the total magnetic force $\vec{F}_m$, and is given by

$$
\begin{aligned}
\vec{F}_m &= \int \vec{f}(\vec{r})\, dV \\
&= \int (\vec{M} \cdot \nabla)\vec{B}\, dV \\
&= \int \left(\frac{\partial \vec{B}}{\partial x} \frac{\partial \vec{B}}{\partial y} \frac{\partial \vec{B}}{\partial z} \right)^{\mathrm{T}} \vec{M}\, dV
\end{aligned}
\tag{1}
$$

Similarly, the magnetic torque $\vec{T}_m$ is given by

$$
\vec{T}_m = \int \mathrm{sk}(\vec{M})\vec{B}\, dV = \mathrm{sk}(\vec{m}_e)\vec{B}
\tag{2}
$$

where $\mathrm{sk}(\vec{M})$ is the skew-symmetric matrix form of the magnetization vector used to express the vector cross-

product in matrix form. As $\vec{T}_m$ is generated via a cross-product, it is impossible to create a magnetic torque that is parallel to $\vec{m}_e$. Thus, existing magnetic microrobots with uniform magnetization profiles cannot be actuated in full six-DOF motion. We assume in this work that the microrobot size is small enough that the field and field gradient are both uniform over the microrobot volume V. Thus, the magnetic force from (1) approximates to $\left(\dfrac{\partial \vec{B}}{\partial x} \dfrac{\partial \vec{B}}{\partial y} \dfrac{\partial \vec{B}}{\partial z}\right)^{\mathrm{T}} \vec{m}_e$ For large values of the field gradient where this uniformity assumption may no longer be valid, the analysis presented here could be extended to account for changes in the field $\vec{B}$ over the volume.

A microrobot with non-uniform magnetization will experience off-axis forces which will induce an unbalanced rigid-body torque. The magnetic torque due to the off-axis magnetization is

$$\vec{T}_o = \int \mathrm{sk}(\vec{r})\vec{f}(\vec{r})\,dV$$
$$= \int \mathrm{sk}(\vec{r})\left(\frac{\partial \vec{B}}{\partial x} \frac{\partial \vec{B}}{\partial y} \frac{\partial \vec{B}}{\partial z}\right)^{\mathrm{T}} \vec{M}\,dV \quad (3)$$

In this study, we are particularly interested in the creation of torque about the $\vec{m}_e$ axis (the missing sixth DOF). The magnitude of the torque about the net magnetization axis $\hat{m}_e$ generated by $\vec{T}_o$, $T_{6-\mathrm{DOF}}$ can be expressed as

$$T_{6-\mathrm{DOF}} = \vec{T}_o \cdot \hat{m}_e = \vec{E}^{\mathrm{T}} \vec{B}_{\mathrm{grad}} \quad (4)$$

where $\vec{E}^{\mathrm{T}} = [e_1\, e_2\, e_3\, e_4\, e_5]$ are coefficients that are functions of $\vec{M}$ and $\vec{r}$. The term $\vec{B}_{\mathrm{grad}}$ represents the independent spatial gradients of $\vec{B}$, and $\vec{m}_e$ is an unit vector parallel to $\vec{m}_e$. Based on Gauss' and Ampere's laws, assuming no electrical current flowing through the workspace, the following relationships must exist between the field gradient terms:

$$\frac{\partial B_x}{dx} + \frac{\partial B_y}{dy} + \frac{\partial B_z}{\partial z} = 0$$
$$\frac{\partial B_x}{\partial y} = \frac{\partial B_y}{\partial x}; \quad \frac{\partial B_x}{\partial z} = \frac{\partial B_z}{\partial x}; \quad \frac{\partial B_y}{\partial z} = \frac{\partial B_z}{\partial y}$$

Thus, out of nine gradient terms, there are only five independent terms, which can be expressed in the local frame as the vector $\vec{B}_{\mathrm{grad}} = \left[\dfrac{\partial B_z}{\partial x} \dfrac{\partial B_z}{\partial y} \dfrac{\partial B_z}{\partial z} \dfrac{\partial B_y}{\partial y} \dfrac{\partial B_x}{\partial y}\right]^{\mathrm{T}}$. Without any loss of generality, there exists a local frame such that the vector $\begin{bmatrix} 0 & 0 & m_e \end{bmatrix}^{\mathrm{T}}$ can be expressed as $\vec{m}_e$. The local frame is intuitive for the design of a robot independent of the actuation coordinates. The generated torques and forces on the microrobot, $\vec{T}_m$, $\vec{F}$ and $T_{6-\mathrm{DOF}}$ can be expressed in this frame as

$$\begin{bmatrix} \vec{T}_m \\ \vec{F} \\ T_{6-\mathrm{DOF}} \end{bmatrix}_{\mathrm{L}}$$
$$= \begin{bmatrix} 0 & -m_e & 0 & 0 & 0 & 0 & 0 & 0 \\ m_e & 0 & 0 & 0 & 0 & 0 & 0 & 0 \\ 0 & 0 & 0 & 0 & 0 & 0 & 0 & 0 \\ 0 & 0 & 0 & m_e & 0 & 0 & 0 & 0 \\ 0 & 0 & 0 & 0 & m_e & 0 & 0 & 0 \\ 0 & 0 & 0 & 0 & 0 & m_e & 0 & 0 \\ 0 & 0 & 0 & e_1 & e_2 & e_3 & e_4 & e_5 \end{bmatrix} \begin{bmatrix} \vec{B} \\ \vec{B}_{\mathrm{grad}} \end{bmatrix}_{\mathrm{L}}$$
$$= \mathbf{D} \begin{bmatrix} \vec{B} \\ \vec{B}_{\mathrm{grad}} \end{bmatrix}_{\mathrm{L}} \quad (5)$$

Here, $\begin{bmatrix} \vec{B} \\ \vec{B}_{\mathrm{grad}} \end{bmatrix}_{\mathrm{L}}$ is also expressed in this local frame (denoted by subscript L) and the matrix $\mathbf{D}$ is defined as the design requirement matrix. Note that the elements of the third row in matrix $\mathbf{D}$ in (5) are all zero which highlights the limitation of existing five-DOF actuation methods, i.e. no torque can be generated about the net magnetization axis $\hat{m}_e$. In order to overcome this limitation and achieve six-DOF actuation capabilities, the last row of $\mathbf{D}$ must be linearly independent from the other rows such that rank($\mathbf{D}$) is six. If this condition is true, it will then be possible to generate a non-zero $T_{6-\mathrm{DOF}}$ to the microrobot independently from the other torques and forces. This implies that either of the coefficients e_4 or e_5 in the last row of $\mathbf{D}$ must be non-zero, which in turn suggests that the magnetization profile must contain components which are non-parallel to $\hat{m}_e$. When rank($\mathbf{D}$) is six, it will be possible for the total torque acting on the microrobot, $\vec{T}$, to have torque about any axis and this total torque can be expressed as

$$\vec{T} = \vec{T}_m + \vec{T}_o = \mathrm{sk}(\vec{m}_e)\vec{B} + \int \mathrm{sk}(\vec{r})\vec{f}(\vec{r})\,dV$$
$$= \mathrm{sk}(\vec{m}_e)\vec{B} + \int \mathrm{sk}(\vec{r})\left(\frac{\partial \vec{B}}{\partial x} \frac{\partial \vec{B}}{\partial y} \frac{\partial \vec{B}}{\partial z}\right)^{\mathrm{T}} \vec{M}\,dV$$
$$(6)$$

2.2. Design methodology and optimization

General design methodologies for magnetic microrobots capable of six-DOF actuation can be developed by ensuring either of the coefficients, e_4 and e_5, in (5) are non-zero. Ideally, the magnitude of these coefficients should also be maximized to enable the highest actuation authority for the microrobots' sixth-DOF. While the control authority depends on both e_4 and e_5, we here present the maximization of either e_4 or e_5, will allow us to show a simple design methodology. This maximization can be achieved by optimizing the orientation of the magnetization profile and
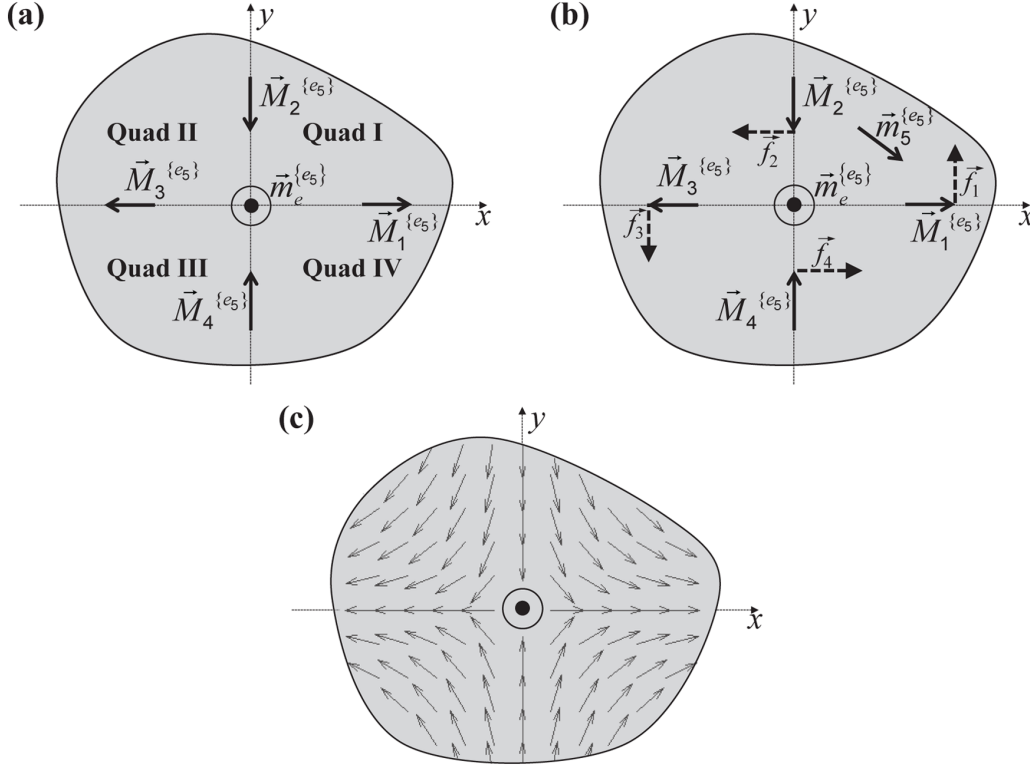
Fig. 2. The design methodology to maximize the e_5 coefficient in (7). (a) The local x–y plane of an arbitrary magnetic microrobot with division into four quadrants (quads I–IV). The microrobot has a net magnetization $\vec{m}_e^{\{e_5\}}$ along its local z-axis and the orientations of the magnetization vectors along the x- and y-axes are illustrated with $\vec{M}_1^{\{e_5\}}$ through $\vec{M}_4^{\{e_5\}}$. (b) When $\frac{\partial B_y}{\partial x}$ is applied, the induced magnetic forces on these magnetization vectors are indicated by the dotted vectors $\vec{f}_1$ to $\vec{f}_4$. A magnetization vector located in quad I can be determined as a weighting function between $\vec{M}_1^{\{e_5\}}$ and $\vec{M}_2^{\{e_5\}}$. (c) The magnetization profile which maximizes the e_5 coefficient.

maximizing its magnitude. The maximum achievable magnetization magnitude is dictated by the material's magnetic properties which we assume can be maximized. Thus, the magnitude of the coefficients e_4 and e_5 can only be further maximized by optimizing the orientation of the magnetization profile. Note that the magnitude of these coefficients can be maximized for either positive or negative absolute values. The difference between these two cases is that the orientation of their magnetization profile are equal but opposite. Thus, for simplicity, this section will only discuss the maximization of the magnitudes of these coefficients as positive values.

In order to maximize e_4 and e_5, their mathematical representations have been derived for a net magnetization in the z-direction, and they can be expressed in their local frame as

$$
\begin{aligned}
e_4 &= \int \left(r_x M_y + r_y M_x\right) dV \\
e_5 &= \int \left(r_x M_x - r_y M_y\right) dV
\end{aligned}
\tag{7}
$$

The variables M_x and M_y represent the x-and y-axes components of $\vec{M}$, respectively. Likewise, the variables r_x and r_y represent the x- and y-axes components of $\vec{r}$, respectively. Equation (7) implies that the requirement to design magnetic microrobots for six-DOF actuation is solely dependent on their local x–y plane's magnetization and geometry. Thus,

without any loss of generality, Figure 2(a) shows the x–y plane of an arbitrarily shaped magnetic microrobot. The geometry of the microrobot can be divided into four quadrants (quads I to IV), and its COM is located at the origin.

As the design process to maximize e_4 and e_5 will lead to two different magnetization profiles, we suggest two different design methodologies where each will only maximize one coefficient. Furthermore, we also introduce a simpler design methodology that can ensure the microrobots will meet sufficient conditions to possess full six-DOF actuation capabilities. Although the simpler design methodology does not maximize e_4 and e_5, it is generally more intuitive. However, note that these proposed design methodologies do not exhaust all possible designs which allow magnetic microrobots to achieve full six-DOF actuation capabilities. We now introduce the three design methodologies.

2.2.1. Maximizing the coefficient e_5. According to the analytical expression of e_5 in (7), the orientations of the magnetization vectors along the x- and y-axes are illustrated with four vectors, $\vec{M}_1^{\{e_5\}}$, $\vec{M}_2^{\{e_5\}}$, $\vec{M}_3^{\{e_5\}}$ and $\vec{M}_4^{\{e_5\}}$ as shown in Figure 2(a). Note that these vectors' orientation are selected such that the integrand in (7) can be maximized. The superscripts, $\{e_5\}$, indicate that these are the required magnetization vectors to maximize the e_5 coefficient.
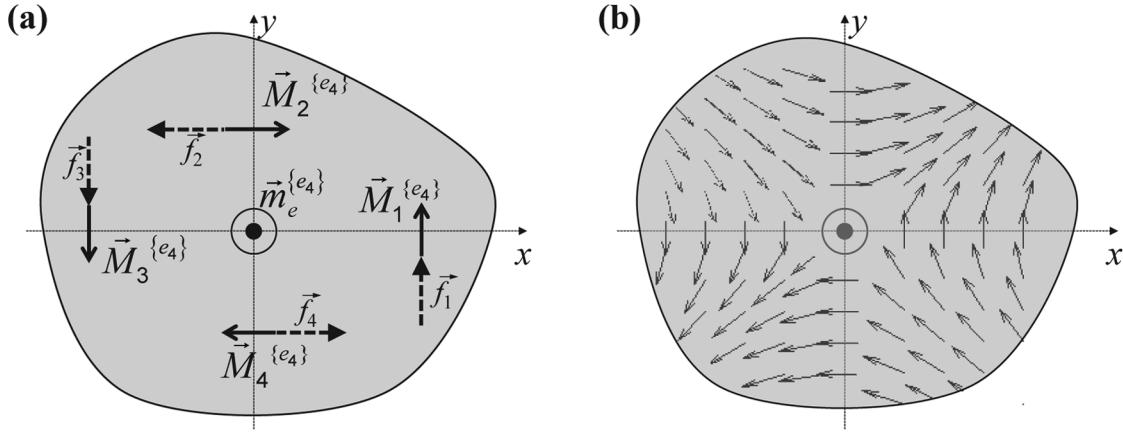
Fig. 3. The design methodology to maximize the e_4 coefficient. (a) The microrobot has a net magnetization $\vec{m}_e^{\{e_4\}}$ along its local z-axis and the orientations of the magnetization vectors along the x- and y-axes are illustrated with $\vec{M}_1^{\{e_4\}}$ through $\vec{M}_4^{\{e_4\}}$. When $\frac{\partial B_y}{\partial x}$ is applied, the induced magnetic forces on these magnetization vectors are indicated by the dotted vectors $\vec{f}_1$ to $\vec{f}_4$. (b) The optimal magnetization profile that can maximize the e_4 coefficient.

When a field gradient $\frac{\partial B_y}{\partial x}$ is applied, the induced magnetic forces on these magnetization vectors are indicated by the dotted vectors shown in Figure 2(b). These induced forces will in turn create rigid-body torques that allow the microrobot to rotate about its positive z-axis (the sixth DOF).

The orientation of the magnetization vector-field in each quadrant can be determined as a weighting function between the magnetization vectors along its adjacent axes. For example, Figure 2(b) shows the required orientation for a magnetization vector, $\vec{M}_5^{\{e_5\}}$, in quadrant I. This vector can be expressed as

$$\vec{M}_5^{\{e_5\}} = k_1 \vec{M}_1^{\{e_5\}} + k_2 \vec{M}_2^{\{e_5\}} \tag{8}$$

where k_1 and k_2 are the weights for $\vec{M}_1^{\{e_5\}}$ and $\vec{M}_2^{\{e_5\}}$, respectively. Both k_1 and k_2 are positive real numbers and their summation is equal to one. The coefficient e_5 can be maximized if the induced magnetic force on $\vec{M}_5^{\{e_5\}}$ is perpendicular to its relative positional vector from the origin. By adjusting the weights appropriately, the optimal orientation of the magnetization profile can be obtained as shown in Figure 2(c). The optimal orientation of the magnetization profile from quadrants I–IV, θ_I to θ_{IV}, can be mathematically described as

$$
\begin{aligned}
\theta_I &= -\tan^{-1}\left(\left|\frac{r_y}{r_x}\right|\right) \\
\theta_{II} &= \tan^{-1}\left(\left|\frac{r_y}{r_x}\right|\right) + \pi \\
\theta_{III} &= -\tan^{-1}\left(\left|\frac{r_y}{r_x}\right|\right) + \pi \\
\theta_{IV} &= \tan^{-1}\left(\left|\frac{r_y}{r_x}\right|\right)
\end{aligned}
\tag{9}
$$

2.2.2. Maximizing the coefficient e_4.
Likewise, based on the analytical expression of e_4, the orientations of the magnetization vectors along the x- and y-axes are illustrated with four vectors, $\vec{M}_1^{\{e_4\}}$, $\vec{M}_2^{\{e_4\}}$, $\vec{M}_3^{\{e_4\}}$ and $\vec{M}_4^{\{e_4\}}$ as shown in Figure 3(a). Similarly, the orientations are selected such that the integrand in (7) is maximized. The superscripts, $\{e_4\}$, indicate that these magnetization vectors are used to maximize the e_4 coefficient.

The induced magnetic forces on the these magnetization vectors when $\frac{\partial B_y}{\partial y}$ is applied, are indicated by the dotted vectors shown in Figure 3(a). These forces enable the microrobot to rotate about its sixth-DOF. Note that the forces $\vec{f}_2$ and $\vec{f}_4$ in Figure 3(a) are created by the induced spatial gradient $\frac{\partial B_x}{\partial x}$ via Gauss' law. As Gauss' law dictates that $\frac{\partial B_x}{\partial x} = -\frac{\partial B_y}{\partial y} - \frac{\partial B_z}{\partial z}$, $\frac{\partial B_x}{\partial x}$ is negatively correlated with $\frac{\partial B_y}{\partial y}$, assuming constant $\frac{\partial B_z}{\partial z}$. Thus, when a positive $\frac{\partial B_y}{\partial y}$ is applied, a negative $\frac{\partial B_x}{\partial x}$ is induced to create $\vec{f}_2$ and $\vec{f}_4$ in Figure 3. The dependence of $\frac{\partial B_x}{\partial x}$ on $\frac{\partial B_z}{\partial z}$ is mathematically represented by e_3 in the **D** matrix.

The orientation of the magnetization profile in each quadrant can be determined as a weighting function between the magnetization vectors along its adjacent axes. The coefficient e_4 can be maximized by adjusting the weights such that the induced magnetic forces are perpendicular to its relative positional vector from the origin. The optimal orientation of the magnetization profile is shown in Figure 3(b) and the optimal orientation of the magnetization profile from quadrants I to IV can be mathematically described as
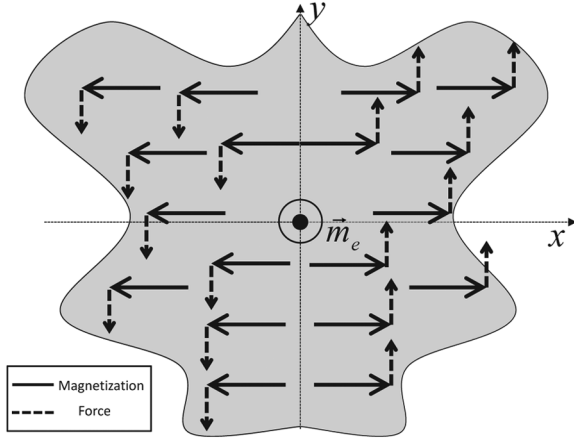
Fig. 4. The intuitive design methodology where the microrobot has a net magnetization $\vec{m}_e$ along its local z-axis and the component of the magnetization vectors in the x–y plane (solid vectors) are always pointing away from the origin. When a spatial gradient $\frac{\partial B_y}{\partial x}$ is applied, the induced force on the magnetization vectors are indicated by the dotted vectors.

$$\begin{aligned}
\theta_I &= \tan^{-1}\left(\left|\frac{r_x}{r_y}\right|\right) \\
\theta_{II} &= -\tan^{-1}\left(\left|\frac{r_x}{r_y}\right|\right) \\
\theta_{III} &= \tan^{-1}\left(\left|\frac{r_x}{r_y}\right|\right) + \pi \\
\theta_{IV} &= -\tan^{-1}\left(\left|\frac{r_x}{r_y}\right|\right) + \pi
\end{aligned} \qquad (10)$$

2.2.3. Intuitive design methodology. A third, more intuitive design methodology can be derived based on the design methodologies in the previous subsections. Although the general design guidelines to maximize e_4 and e_5 are different, they share a common trait: their $x - y$ plane's magnetization profile are anti-symmetrical about the origin. Based on this trait, it should be noted that the sufficient conditions to possess all full six-DOF can be satisfied if the magnetization profiles are either always pointing towards or away from the origin. Furthermore, the design of the microrobot can be further simplified if it is geometrically symmetric. Thus, Figure 4 shows a generic microrobot with symmetrical features that can possess all six-DOF actuation by having the magnetization profile (solid vectors) to always point away from the y-axis. Note that the sixth-DOF of the microrobot shown in Figure 4 can be actuated with $\frac{\partial B_y}{\partial x}$. When a positive $\frac{\partial B_y}{\partial x}$ is applied, all the magnetization vectors at the right half plane of the microrobot will experience a force in the $+y$-direction. Concurrently, all the magnetization vectors at the left half plane will experience a force in the $-y$-direction. These induced magnetic forces are indicated by the dotted vectors in Figure 4 and they will create a net rigid-body torque about the $+z$-axis that allow the microrobot to rotate about its sixth DOF.

2.3. Control of magnetic fields and gradients

The magnetic field and its spatial gradients depend linearly on the currents through the coils (Kummer et al., 2010), and the field and gradient terms can be expressed as

$$\vec{B} = \mathbf{B}\vec{I} \qquad (11)$$

$$\frac{\partial \vec{B}}{\partial x} = \mathbf{B}_x \vec{I}; \quad \frac{\partial \vec{B}}{\partial y} = \mathbf{B}_y \vec{I}; \quad \frac{\partial \vec{B}}{\partial z} = \mathbf{B}_z \vec{I} \qquad (12)$$

where each element of $\vec{I}$ is current through each of the c coils, $\mathbf{B}$ is a $3 \times c$ matrix mapping these coil currents to the magnetic field vector $\vec{B}$ and $\mathbf{B}_x$, $\mathbf{B}_y$, $\mathbf{B}_z$ are the $3 \times c$ matrices mapping the coil currents to the magnetic field spatial gradients in the x, y and z directions, respectively. In this work, these mapping matrices are calculated for a given coil arrangement by treating the coils as magnetic dipoles in space and are calibrated through workspace measurements (Meeker et al., 1996; Kummer et al., 2010).

Thus, for a desired torque and force on a single magnetic microrobot with a net magnetic moment $\vec{m}_e = \int \vec{M}\, dV$ we use (1) and (6) to arrive at

$$\begin{bmatrix} \vec{T} \\ \vec{F} \end{bmatrix} = \begin{bmatrix} \mathrm{sk}(\vec{m}_e)\mathbf{B} + \int \mathrm{sk}(\vec{r}) \begin{bmatrix} \vec{M}^{\mathrm{T}}\mathbf{B}_x \\ \vec{M}^{\mathrm{T}}\mathbf{B}_y \\ \vec{M}^{\mathrm{T}}\mathbf{B}_z \end{bmatrix} dV \\ \vec{m}_e^{\mathrm{T}}\mathbf{B}_x \\ \vec{m}_e^{\mathrm{T}}\mathbf{B}_y \\ \vec{m}_e^{\mathrm{T}}\mathbf{B}_z \end{bmatrix} \vec{I} \qquad (13)$$

$$= \mathbf{A}\vec{I}$$

where $\mathbf{A}$ is the $6 \times c$ matrix mapping the coil currents $\vec{I}$ to the torque $\vec{T}$ and force $\vec{F}$. Equation (13) can be solved assuming $\mathbf{A}$ is full rank, i.e. the number of coils c is greater than or equal to 6 and the system is not experiencing any orientation-dependent singularities. The full solution can be accomplished for $c \neq 6$ through the pseudo-inverse, which finds the solution that minimizes the 2-norm of $\vec{I}$ as

$$\vec{I} = \mathbf{A}^+ \begin{bmatrix} \vec{T} \\ \vec{F} \end{bmatrix} \qquad (14)$$

If $c < 6$, then the solution would be a least-squares approximation. Having greater than six coils leads to a better conditioned $\mathbf{A}$ matrix, which means a more isotropic workspace, reduction of singularity configurations and lower coil current requirements. With knowledge of the orientation state of the microrobot, one can then solve (13) in order to achieve any desired actuation force and torque.

3. Discrete magnet and continuous magnetization configurations

We now consider several special cases of magnetization profile. First we consider microrobot bodies with discrete regions of uniform magnetization, as is common in permanent-magnet microrobots. Then we will consider

microrobots with continuously varying magnetization, as is common in non-permanent (soft) microrobots.

3.1. Discrete magnet configurations

In order to reduce the fabrication complexity for permanent-magnet microrobots, the distributed magnetization profile can be simplified into discrete elements with uniform magnetization. To simplify the model, we assume that such discrete magnet elements can be modeled as magnetic dipoles. Two different discrete models (two- and three-magnet configurations) will be introduced and discussed in this section. Both configurations will consist of one main magnet that permits the microrobot to achieve the usual five DOFs, and additional magnets which enable the sixth DOF. The microrobot orientation is defined by the orientation of the main magnet $\vec{m}$. Note that the three-magnet configuration is designed based on the "intuitive design methodology" shown in Section 2.2 while the two-magnet configuration does not follow any design methodologies. Thus, the purpose of introducing two different types of configuration is to highlight the benefits of the proposed design methodology shown in Section 2.2.

Similar to the continuous magnetization profile case discussed in Section 2, any combination of discrete magnets which satisfy the requirement of rank($\mathbf{D}$) = 6 in (5) will result in six-DOF actuation capability. To get the most actuation authority in the sixth-DOF, the discrete magnets should be placed perpendicular to each other so as to maximize the torque about $\vec{m}_e$. We introduce the simplest possible design, the two-magnet configuration, which can achieve all six-DOF actuation capability.

3.1.1. Two-magnet configuration. The simplest configuration, the two-magnet configuration, is illustrated in Figure 5(a) where two magnets of magnetic dipole strength $\vec{m}$ and $\vec{m}_2$ are separated by a vector $\vec{r}_2$. Note that the magnet with magnetization vector $\vec{m}$ is the main magnet and it is perpendicular to $\vec{m}_2$. The COM is assumed to be located at the main magnet and thus the magnetic torque and force acting on the microrobot can be expressed by

$$
\begin{bmatrix} \vec{T} \\ \vec{F} \end{bmatrix} = \begin{bmatrix} \mathrm{sk}(\vec{m}+\vec{m}_2)\mathbf{B} + \mathrm{sk}(\vec{r}_2)\begin{bmatrix} \vec{m}_2^\mathrm{T}\mathbf{B}_x \\ \vec{m}_2^\mathrm{T}\mathbf{B}_y \\ \vec{m}_2^\mathrm{T}\mathbf{B}_z \end{bmatrix} \\ \vec{m}^\mathrm{T}\mathbf{B}_x + \vec{m}_2^\mathrm{T}\mathbf{B}_x \\ \vec{m}^\mathrm{T}\mathbf{B}_y + \vec{m}_2^\mathrm{T}\mathbf{B}_y \\ \vec{m}^\mathrm{T}\mathbf{B}_z + \vec{m}_2^\mathrm{T}\mathbf{B}_z \end{bmatrix} \vec{I} \quad (15)
$$

Thus, similar to the continuous magnetization case, the two-magnet configuration can also achieve six-DOF actuation. However, it is noted that (15) could be simplified by following the intuitive design methodology shown in Section 2.2 by adding more magnets to create a symmetric arrangement. Specifically, the contribution of $\vec{m}_2$ to the rigid-body force could be canceled with the addition of one more magnet.

(a) two-magnets

(b) three-magnets
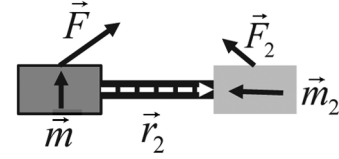
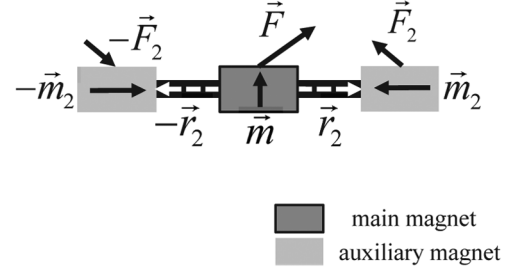main magnet
auxiliary magnet

Fig. 5. The schematic of the two- and three-magnet configurations are shown in (a) and (b), respectively. In both configurations, the main magnet's magnetization vector is represented by $\vec{m}$ while the rest of the magnets are auxiliary magnets. In (b), the vectors $\vec{m}$ and $\vec{m}_2$ are orthogonal to one another and the magnets are placed collinearly. The auxiliary magnets have equal and opposite magnetization vectors.

3.1.2. Three-magnet configuration. The coupling between the magnets can be reduced by using the intuitive design methodology in Section 2.2, to develop the three-magnet configuration as shown in Figure 5(b). In order to obey these design guidelines, the auxiliary magnets and the main magnet are placed collinearly and the main magnet is located at the center. The auxiliary magnets are magnetized in such a way that they are equal and opposite, i.e. $\vec{m}_2$ and $-\vec{m}_2$. The magnetization vector of the main magnet, $\vec{m}$, is orthogonal to $\vec{m}_2$.

Due to the symmetrical arrangement, the net magnetic moment of the microrobot is aligned with the main magnet $\vec{m}$, and the auxiliary magnets contribute only to the rigid-body torque. Magnetic forces on the auxiliary magnets are equal and opposite, thus canceling out. The actuation is thus written as

$$
\begin{bmatrix} \vec{T} \\ \vec{F} \end{bmatrix} = \begin{bmatrix} \mathrm{sk}(\vec{m})\mathbf{B} + 2\mathrm{sk}(\vec{r}_2)\begin{bmatrix} \vec{m}_2^\mathrm{T}\mathbf{B}_x \\ \vec{m}_2^\mathrm{T}\mathbf{B}_y \\ \vec{m}_2^\mathrm{T}\mathbf{B}_z \end{bmatrix} \\ \vec{m}^\mathrm{T}\mathbf{B}_x \\ \vec{m}^\mathrm{T}\mathbf{B}_y \\ \vec{m}^\mathrm{T}\mathbf{B}_z \end{bmatrix} \vec{I} \quad (16)
$$

The number of terms contributing to the force $\vec{F}$ are thus reduced in this decoupled case, simplifying the analysis. However, it should be noted that the auxiliary magnets are still contributing to torques about all three axes. The rigid-body torques created by these magnets that are non-parallel

to the sixth DOF, however, can be canceled by adjusting the magnetic torque acting on the main magnet.

3.2. Non-permanent (soft) magnetization profiles

The previous sections of this study have not specified if the magnetic body of the microrobot is a permanent (hard) or non-permanent (soft) magnet. The magnetization of a hard magnet is not affected by applied fields during actuation (assuming the fields remain under the magnet's coercivity value), but a soft-magnet body will experience changes in magnetization as the applied actuation field direction or magnitude is changed. The analysis presented in the previous section is indeed appropriate for hard or soft magnets, but presumes that the magnetization throughout the magnetic volume is known. The discrete magnet cases presented assume volumes with uniform magnetization, a state which is closely approximated in hard magnetic materials which preserve their magnetization even when any externally applied field is changed or removed. For soft magnets, the internal magnetization of the body is a function of the applied field, the magnetic susceptibility χ, and the magnet shape. In this section, we provide a formulation for the magnetization within a soft magnet body, and study a class of soft magnet bodies whose magnetization can be treated in a similar manner to that of permanent magnets. A full study on general soft magnet bodies in relation to six-DOF control is left to future work.

The magnetization of a soft magnetic body will be influenced by fields internal to the body, known as demagnetizing fields. This internal demagnetizing field $\vec{H}_d$ acts in a direction opposite to the magnetization $\vec{M}$ inside the body. Thus, the true field $\vec{H}_{tr}$ inside the magnetic body depends on the applied field $\vec{H}_a$ and the demagnetizing field $\vec{H}_d$ as

$$\left|\vec{H}_{tr}\right| = \left|\vec{H}_a\right| - \left|\vec{H}_d\right| \tag{17}$$

The magnetization of the soft material can be related to the external magnetic field $\vec{B}$ and the true field by

$$\vec{M} = \frac{\vec{B}}{\mu_o} - \vec{H}_{tr} \tag{18}$$

The magnetization of the soft material can be approximated (in its pre-saturation regime, where it is assumed $\vec{B} = \mu \vec{H}_{tr}$) to be linearly related to the true field by the susceptibility χ as

$$\vec{M} = \vec{H}_{tr}\left(\frac{\mu}{\mu_o} - 1\right) = \chi \vec{H}_{tr} \tag{19}$$

For a magnetic material with relative permeability $\mu/\mu_0 > 1$, the magnetic flux in the region outside the magnet tends to crowd into the magnet (Cullity and Graham, 2008). A higher permeability of the magnetic material results in a higher distortion of the field and thus a higher magnetization $\vec{M}$. The demagnetizing field is proportional to the internal magnetization, and related by the demagnetizing coefficient N_d as

$$\vec{H}_d = -N_d \vec{M} \tag{20}$$

The value of N_d can be found exactly for an ellipsoid, but can be approximated for other shapes. Values for cylinders, rods and disks are given in Cullity and Graham (2008). The distribution of the demagnetizing fields inside the magnet body is highly dependent on the geometry of the magnet. This magnetic anisotropy can be influenced by other factors such as the crystalline structure, magnetoelastic effects, and interactions between different magnetic materials. However, we assume that due to the size and homogeneity of the microrobot structures that the shape demagnetizing factor will dominate. An ellipsoidal magnet body will result in a uniform demagnetizing field $\vec{H}_d$ and thus a uniform magnetization $\vec{M}$. However, any other magnet geometry will necessarily result in non-uniform magnetization within the body under a uniform applied field $\vec{H}_a$. Combining (17) through (20), we get a solution for the magnetization as a function of the applied field and the demagnetizing factor as

$$\left|\vec{M}\right| = \frac{\chi\left|\vec{H}_a\right|}{1 - \chi N_d} \tag{21}$$

This solution approximates the magnetization as constant within the magnetic body, and is thus not suitable for application to the present work. Thus, a finite element simulation which uses the above governing relations to find the magnetization throughout the microrobot body is used to study complex soft microrobot shapes with non-uniform magnetization.

Long thin shapes such as long rods result in large demagnetizing fields perpendicular to the long axis of the shape, leading to net magnetization which tends to align with the rod's long axis. This gives potential for a highly distorted magnetization profile from the direction of applied field. This fact can be used to design a microrobot shape with highly non-uniform magnetization for six-DOF actuation. To achieve a magnetization profile with two regions of nearly perpendicular magnetization, a geometry such as that shown in Figure 6 can be used. The figure shows the internal magnetization within this shape under a uniform applied field. The A region contributes a positive *z*-magnetization and negative *x*-magnetization while the B region contributes a positive *x*-magnetization as well as a positive *z*-magnetization. Thus, the magnetization profile can be approximated as three regions each with uniform magnetization arrange perpendicular to one another, similar to the discrete magnet case studied in Section 3.1.2. Each region contains a portion that contributes only a positive *z*-magnetization. This additional magnetization provides stability to the microrobot if the microrobot is not initially aligned with the magnetic field. Many other geometries could achieve non-uniform magnetization profiles which
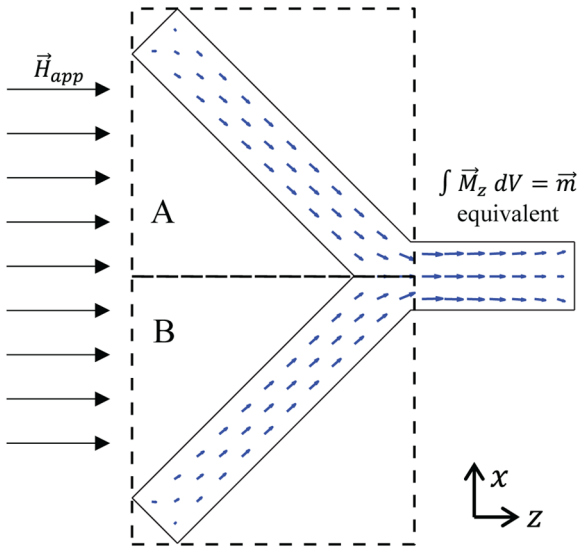
Fig. 6. Magnetization profile found using finite element analysis (COMSOL 4.0) inside a soft magnetic material with relative permeability $\mu/\mu_0 = 100$ when placed in a uniform applied field $\vec{H}$ of magnitude 15.9 kA/m such that the material is not magnetically saturated. The two shaded regions show the division of the magnetization in the x-direction into the two directions analogous to the side magnets.

satisfy the sufficient conditions, the designs of which are dependent on the desired application. These designs are able to achieve full six-DOF actuation.

If the material is driven into its saturation region, the magnetization-field linearity assumption will be invalid. In addition, the magnetic domains will completely align with the magnetic field, reducing then eliminating the non-uniform magnetization profile. Thus, the microrobot would ideally be made from a material with a large linear magnetization region, requiring a large applied field to drive it to saturation. In addition, the magnetization inside a non-spherical soft-magnet body will depend on the direction of the applied field. Thus, any control strategy for six-DOF control which requires precise knowledge of the magnetization profile would require feedback of the body orientation while remaining in the linear magnetization region of the material. Then the magnetization could be found using finite element analysis or using an analytical approximation using demagnetizing factors calculated for the shape. Feedback control and optimization of such a shape is left to future work. These microrobots can be fabricated using the methods presented in previous work (Imbaby et al., 2008; Pawashe et al., 2009). In addition, alternative micro-fabrication methods such as electroplating can be explored for materials such as nickel (Kummer et al., 2010).

4. Control

As discussed in Section 2, to apply a desired six-DOF wrench to the rigid body, the three-DOF orientation of the body must be known through feedback. If the three-DOF orientation is known, a six-DOF wrench can be applied using (13). However, the requirement for such orientation feedback is burdensome in an experimental implementation. For the previously established five-DOF control, such a limitation is overcome by commanding the field direction rather than specifying desired torques. The assumption was made that the magnetization direction of the microrobot would quickly orient to the direction of the field. The advantage of this over torque-based control is that the orientation of $\vec{m}$ need not be tracked. As this specifies the vector $[\vec{B}\,\vec{F}]^{\mathrm{T}}$ we call this BF mode. The previous section introduced microrobot designs that would allow a microrobot with non-uniform magnetization to be controlled using this control strategy.

4.1. Open-loop rotation control

To overcome the orientation limitation and incorporate the open-loop strategy of BF mode, one would want to specify the field, rigid-body force, and off-axis torque. However, these cannot each be specified at the same instant in time. This arises from the fact that the rigid-body torque can be written as a linear combination of individual forces and the applied magnetic field. The actuation matrix would then be overdetermined and not full rank. However, the actuation matrix could be solved for a combination of two of the three desired vectors. In the open-loop rotation control scheme, a torque about the magnetization axis and desired force is specified. Orientation only for the magnetization axis is required. Additional dynamic effects (e.g. fluid flow, gravity) could apply a torque on the other two axis of rotation. In addition, the resulting magnetic field will have a minor, but significant contribution to this undesired torque. We designate this TF mode as the controller specifies the vector $[\vec{T}\,\vec{F}]^{\mathrm{T}}$.

It is important to reiterate that TF mode can specify torques orthogonal and parallel to the magnetization axis, but without knowledge of the orientation of the affected axis, these could produce undesired effects. A second rotation axis could be tracked to give five-DOF control in TF mode, and the third orientation would achieve all six DOFs. In this work when we discuss TF mode, we will be discussing the case of feedback only about the magnetization axis.

4.2. Hybrid mode

A compromise between TF and BF modes can be reached which results in reduced orientation feedback requirements. In this hybrid mode, the controller alternates between BF and TF modes as needed to control all six DOFs. BF mode is used nominally as an open-loop five-DOF controller, without control over the sixth DOF. Periodically, the controller switches to TF mode to exert a desired torque on the sixth DOF. When in TF mode, the controller assumes that the two orientation states ensured by BF mode remain constant. Thus, the controller only requires feedback from one

orientation axis. The controller will only remain in TF mode for a short time to ensure that the other five DOF can be assumed as unaffected. This length of time will be dependent on the accuracy of the feedback and control system and the presence of disturbance forces.

We can calculate the resulting field, force, or torque for any set of coil currents $\vec{I}$. We can then calculate the resulting non-zero torque for BF mode and the resulting magnetic field for TF mode. Ideally, these would be zero, except for the case of TF mode, for which we would desire a non-zero field in the direction of the magnetization axis. It is observed that BF mode would contribute non-negligible torque about the magnetization axis. This agrees with qualitative observations in previous work. In TF mode, the resulting magnetic field is small compared with typically applied field magnitudes, however the direction of the field deviated only slightly from the magnetization axis. This indicates TF mode will keep the direction of the magnetization axis. However, in experiments, the field is non-uniform and $\vec{I}$ is solved for the workspace center. The small field magnitude and large gradients generated to produce the torque and force mean that there is a high probability the microrobot will not experience the correct low-magnitude resultant field.

It is also important to note the remaining combination of desired vectors which could define a control mode, that of a field and a torque, which would be designated BT. This mode would ensure the magnetization axis would be fixed and would specify the torque about it. Under the current control strategy, this would be redundant as the TF mode will generally keep the direction of the magnetization constant. Tests of this mode showed that for typical fields and torques, magnetic forces upwards of 15 nN would be applied on a microrobot of magnetization 1.0 μAm^2. While this force will produce some translational motion on a microrobot, typical desired forces are an order of magnitude greater.

5. Experiments

5.1. Fabrication and actuation

Microrobots containing discrete permanent magnets are fabricated in several pieces and fixed together using an adhesive. Individual magnet elements are fabricated to be magnetically hard, retaining their internal magnetization in the absence of an externally applied magnetic field, or magnetically soft, with magnetization dependent on the applied field. Microrobots are fabricated in a batch process using soft photolithography and molding techniques in a manner similar to techniques for micro-scale robots and parts (Imbaby et al., 2008; Diller et al., 2011). The shape is chosen as rectilinear solid, but could be chosen arbitrarily to suit a particular application. Microrobot magnetic elements are composed of neodymium–iron–boron (NdFeB) particles in a polyurethane matrix. Due to the high magnetic coercivity of NdFeB (i.e. fields over 600 mT are
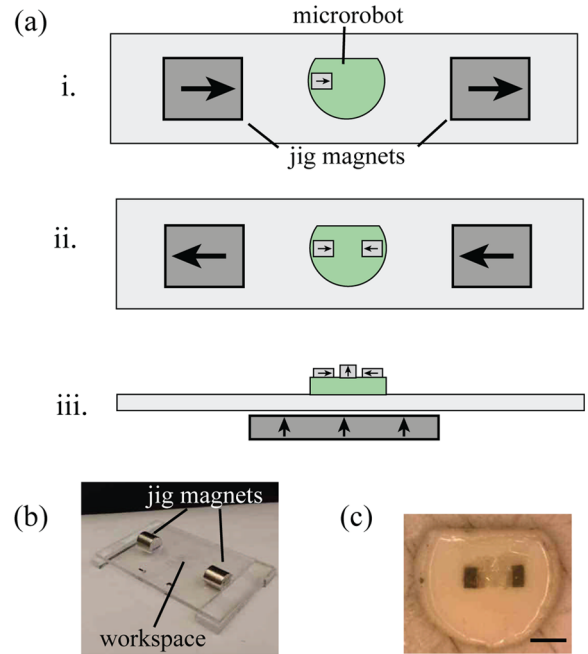

Fig. 7. (a) Module assembly. (i) First magnet is affixed to the microrobot body and aligned. (ii) Jig magnets are flipped and the second magnet is affixed to the body. (iii) The jig magnets are removed, a magnet is placed underneath the jig and the center magnet is affixed to the body. (b) Assembly jig with alignment magnets. (c) Assembled module with two magnets of opposing magnetization. Note that the arrows represent the magnets' magnetization vector. Scale bar is 1 mm.

required to demagnetize NdFeB), these microrobots are not subject to demagnetization from the relatively weak fields applied in this work. The molding process for the magnetic elements is prone to variations in microrobot geometry (up to about 10 % from nominal), but the control method is not sensitive to small geometric changes. To achieve decoupled actuation, each magnetic element must have the same magnetic moment strength. This is ensured by magnetizing each element individually in an alternating gradient force magnetometer (AGFM, Micromag 2900) to a strength of $1.64 \pm 0.01 \ \mu Am^2$.

The discrete magnetic elements are mounted to a molded polyurethane base or an acetal base which is laser-cut from a flat sheet. The nature of the material is not important from a magnetic actuation standpoint, but does provide a base upon which to precisely align the magnetic elements, and offers a shape for computer vision detection. The shape chosen for experimental demonstrations is shown in Figure 7, and consists of a circle with a flat edge for ease of vision detection. The relative orientation of each magnet element in the microrobot is critical to achieve accurate control based on (16), and so the magnets are placed one-at-a-time with a magnetic alignment jig, as shown in Figure 7(a) for the example microrobot with reduced coupling shown in Figure 5(b). This design consists of three magnetic elements which must be aligned
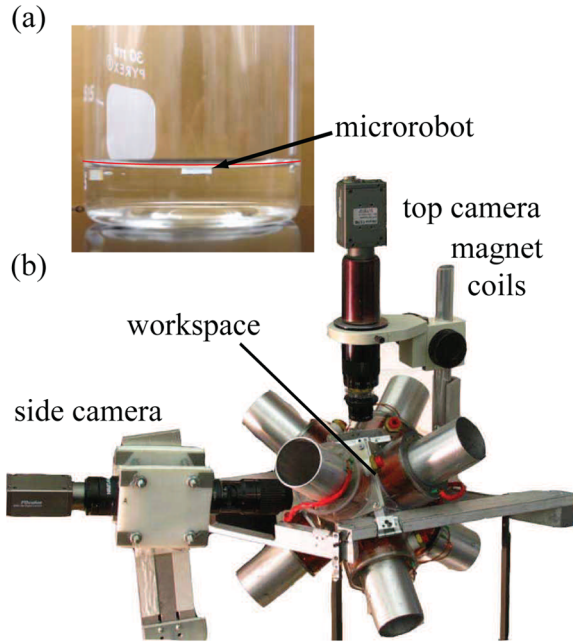
(a)

(b)

Fig. 8. (a) Shape of water meniscus. The meniscus shape is predicted by (22). (b) Photograph of the electromagnetic coil setup. All system components are shown with the coils in the operational position. Two coils hinge open to allow for access to the workspace.

perpendicular and anti-parallel to each other. In Figure 7(a,i), the first module is placed pointing to the right. The jig magnets provide an aligning field to ensure that the element is aligned with minimal error. The module is held in place with UV-curable adhesive (Loctite 3761) so that it can be cured with a UV light source after alignment is ensured. In Figure 7(a,ii), the jig magnets are reversed and the second magnet is placed and fixed. In Figure 7(a,iii), an out-of-plane jig magnet is used to place the final magnetic element pointing in the upward direction. Once all magnetic elements are placed, the microrobot is removed from the jig and can be placed in a liquid environment for actuation. A photograph of the aligning jig is shown in Figure 7(b) and the completed microrobot is shown in Figure 7(c).

The magnetic microrobots are actuated by eight independent air or iron-core electromagnetic coils shown in Figure 8, which are aligned pointing to a common workspace center point with an approximate opening size of 12 cm. The currents in the electromagnetic coils are controlled using a PC with data acquisition system at a control bandwidth of 20 kHz, using linear electronic amplifiers (SyRen 25, Dimension Engineering Inc.) and Hall-effect current sensors (ACS714, Allegro Microsystems Inc.). Imaging of the microrobots and workspace is accomplished by two CCD cameras (Foculus F0134SB) connected to variable magnification microscope lenses, providing up to a 26 mm × 20 mm field of view from the top and side perspectives. Magnetic flux densities and gradients of up to

8.3 mT and 0.34 T/m, respectively, can be generated in the workspace, with a $3.3 \times$ increase when iron cores are inserted into the coils. For a 20 mm × 20 mm × 20 mm workspace in the center of the coil system, the field and field gradient are shown to be uniform within 6.0% of the nominal values as measured with a Hall effect sensor (Lakeshore Gaussmeter 410).

5.2. Orientation detection

The orientation of the microrobot about the magnetization axis is accomplished using visual feedback with OpenCV software. Hough transforms are used to identify the center of the circular shape and the endpoints of the flat edge of the microrobot body. To ensure precise and accurate object detection, the workspace is back-lit to create a high-contrast silhouette of the microrobot for the top-camera view. The detection algorithm returns the center position of the microrobot and its orientation once per video frame. For the experiments shown in this work, we assume that the microrobot is oriented so that the top or side camera is directly viewing one of the flat faces of the microrobot. This constraint could be relaxed for general rotations if both cameras are used simultaneously for orientation detection.

5.3. Experimental results

5.3.1. Water surface actuation results. To test the coupling, the microrobot is actuated using the TF control method on the water surface. This is done to restrict rotation about the axes normally controlled by open loop five-DOF control and can yield unpredictable results in TF mode as discussed in Section 4.1. The water surface also restricts z-axis motion, and reduces surface interactions which affect motion of the microrobot. A controller to alternate between the modes is not required.

To minimize surface energy, a meniscus forms on the water-air interface and satisfies the linearized Laplace equation, which is solved by

$$h(x, y) = x_c \cot(\theta_c)\operatorname{csch}\left(\frac{R}{x_c}\right) \cosh\left(\frac{\sqrt{x^2 + y^2}}{x_c}\right) \quad (22)$$

where x_c is the characteristic capillary length, θ_c is the contact angle of the container (glass), and R is the radius of the cylindrical container (Hosokawa et al., 1996).

The meniscus will oppose displacement of the microrobot on the water surface. When the microrobot is at a steady state displacement, the forces of the meniscus on the microrobot are

$$\begin{aligned} F_x(x) &= m_r g \frac{\partial h(x, y)}{\partial x} \\ F_y(y) &= m_r g \frac{\partial h(x, y)}{\partial y} \end{aligned} \quad (23)$$

where m_r is the effective mass of the microrobot after accounting for the bouyant force.

The microrobot will experience drag due to being on the water surface and follows the drag form equation,

$$\vec{T}_d = C_d \vec{\omega}^2 \tag{24}$$

where ω is the rotational velocity of the microrobot. The drag coefficient, C_d, is found to be $4.2 \times 10^{-10} \pm 5.4 \times 10^{-22}$ N.m.s^2 by a first-order least-squares fit of the observed ω^2 for a given torque. Variations in the drag coefficient will affect the magnitude of the observed torque for a given observed rotation rate, but will not affect the observed decoupling between the torque and the translation forces.

In the experiment, the controller sweeps through steps of forces or torques. At each force or torque, 5 s is allowed for steady-state position or rotation rate to be achieved, and the state is recorded. Between each experiment, 60 s are allowed for the coils to cool. Figure 9 and Multimedia Extension 1 show the results of independently applied torque about the z-axis, and force in the x- and y-directions and the observed resulting force or torque. The slopes of the fitted lines correspond to the reported coupling matrix. An ideal microrobot would produce plots with slopes of 1 in the diagonal plots and slopes of 0 on the off-diagonal plots.

As the forces and torques on the water surface are difficult to model accurately, experimental error is expected. The model is very sensitive to environment parameters, especially the container–water contact angle, microrobot–water contact angle, and microrobot weight. However, errors in these parameters would scale the observed forces and torques proportionally across an experiment. In the experimental analysis, we are primarily interested in the ratio between desired and undesired actuations, so these proportional scalings will not affect the results.

We study the ratio of these actuations by looking at the magnitude of each observed motion when one actuating force or torque is desired. This is represented by the coupling matrix

$$\begin{bmatrix} \dfrac{\partial T_\theta}{\partial T_\theta} & \dfrac{\partial T_\theta}{\partial F_x} & \dfrac{\partial T_\theta}{\partial F_y} \\[2mm] \dfrac{\partial F_x}{\partial T_\theta} & \dfrac{\partial F_x}{\partial F_x} & \dfrac{\partial F_x}{\partial F_y} \\[2mm] \dfrac{\partial F_y}{\partial T_\theta} & \dfrac{\partial F_y}{\partial F_x} & \dfrac{\partial F_y}{\partial F_y} \end{bmatrix} \tag{25}$$

To allow for comparison of forces with torques in the coupling matrix, the torques are scaled by dividing by the length moment arm of the microrobot, 2 mm. The diagonal terms of the coupling matrix represent the desired motions, while the off-diagonal terms represent undesired motions which are coupled to actuation. When the microrobot magnetization $\vec{M}(\vec{r})$ is known and (13) is solvable, then the coupling matrix should be the identity matrix. The scale of the off-diagonal terms give the coupling of the system.

Thus, we can look at the relative magnitude of the diagonal and off-diagonal terms to determine the precision of actuation. To further aid comparison, each row of the coupling matrix is scaled such that the diagonal terms are unity, eliminating error from the rotational drag and meniscus models. For the data shown in Figure 9, The coupling matrix is found to be

$$\begin{bmatrix} 1 & 4.9 \times 10^{-5} & 1.1 \times 10^{-5} \\ 3.0 \times 10^{-2} & 1 & -1.7 \times 10^{-2} \\ 2.3 \times 10^{-2} & 4.9 \times 10^{-2} & 1 \end{bmatrix} \tag{26}$$

The worst coupling factors are the forces in x and y that correspond to the desired y- and x-forces, respectively. These coupling errors can be due to the sensitivity in camera mounting with respect to the workspace and placement of the microrobot in the workspace. Despite this, the worst-case coupling is that of the x-displacement response when experiencing a y-force, with a response 20 times less than that of the y-displacement response.

5.3.2. Immersed six-DOF actuation. A second, neutrally buoyant microrobot is used to qualitatively demonstrate unconstrained six-DOF control in a fluid. The three-magnet microrobot is fabricated as described in Section 5.1, with the exception that the polymer body is fabricated to have a density less than that of water by inclusion of hollow glass microbeads (3M K1). Additional weights are manually added to the underside of the microrobot (the side with the aligned magnets) until the overall density approached that of high viscosity 50 cSt silicone oil. The high viscosity oil is used to slow the motions for observation in this demonstration. Independent actuation of each DOF is then applied one-at-a-time to the microrobot and recorded. Here, visual feedback is only required for torque about the z-axis.

Snapshots of the motions can be seen in Figure 10, with a full video found in Multimedia Extension 1. The left-hand side shows the side camera views for rotation about the x- and y-axes and z-axis translation. The right-hand side shows the top camera view for x- and y-axes translation and rotation about the z-axis. An outline of the neutral starting position is given for reference. The y- and z-translations exhibit minor rotation about the magnetization axis, which is expected as there is no control about that axis. The various rotations exhibit minor x and y motion. All motions except for the controlled z translation gradually move in the negative z-direction due to gravity. Due to the higher current requirements of applying fields and forces in the same direction (Kummer et al., 2010), the microrobot is oriented in the x-direction for the x- and z-translations, and the z-direction for the y-translation. The only feedback used is to determine the direction of $\vec{m}_2$ for the rotation about the magnetization axis. The remainder of the motions are controlled via a teleoperated open-loop controller. As the polymer body is fabricated to have a density less than the oil and all masses with density greater than that of oil on one side of the body, buoyant forces allow for
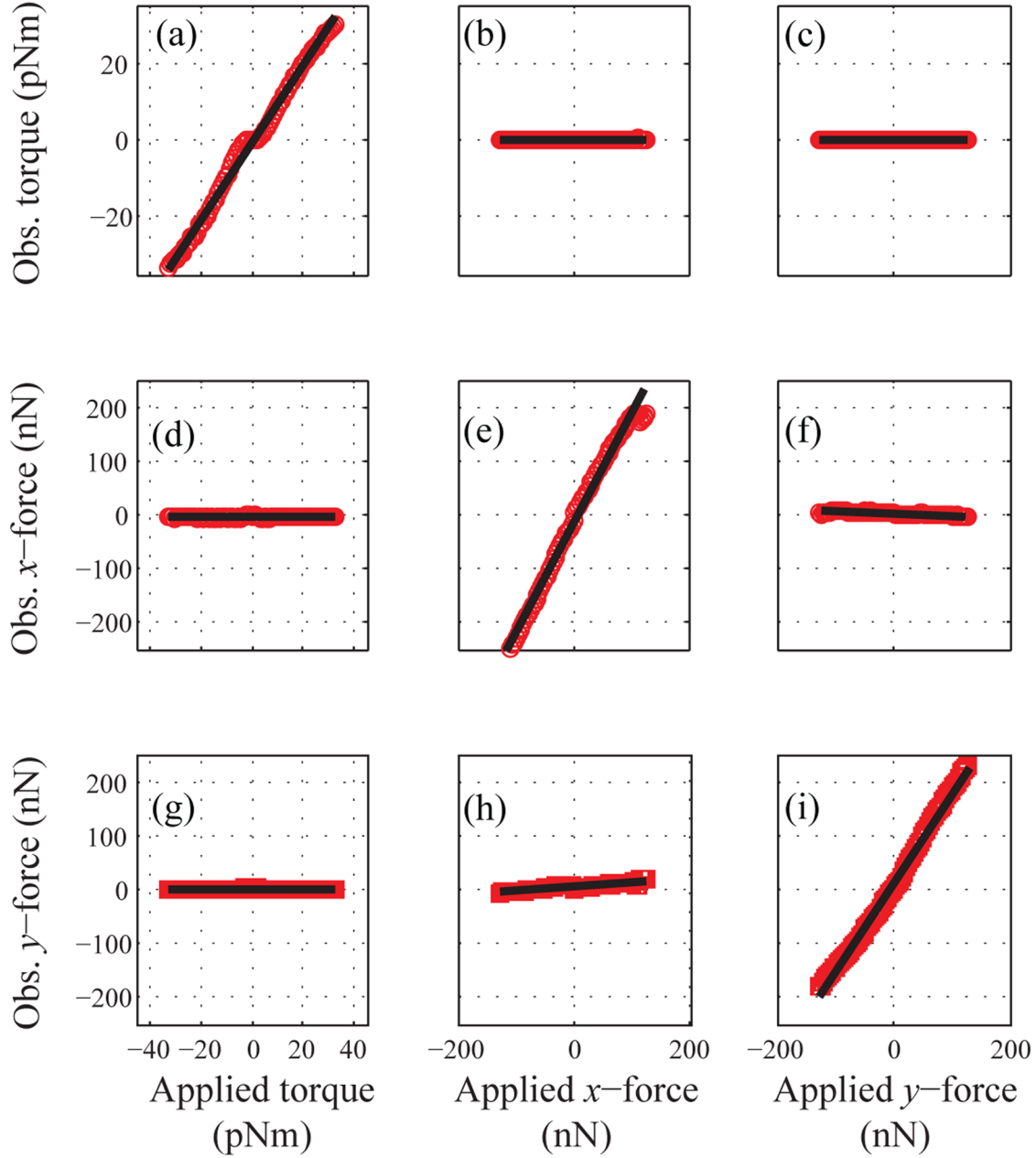
Fig. 9. Coupling of the forces in the *x-y* direction and torque about the *z* axis for a microrobot operating on the water surface. Each plot corresponds to an element in (25). The rows correspond to the torque (a-c), *x*-force (d-f), and *y*-force (g-i) response to an independent desired torque (left column), *x*-force (center column), and *y*-force (right column). In this example $m = 0.64 \pm 0.01 \mu Am^2$ and $m_2 = 1.64 \pm 0.01 \ \mu Am^2$. For this microrobot design, the creation of T_{6-DOF} as introduced in (4) is dictated by the vector $\vec{E} = [0\ 0\ 0\ 0 - 2m_2 r]^T$, where $r = 1$ mm is the side-magnet spacing. A video of this motion is shown in Multimedia Extension 1.

the microrobot to "self-right". This is beneficial for experiments as the microrobot would naturally align itself such that the primary magnet would point towards the top camera for angle detection for the rotation about the *z*-axis. However, the magnetic torque will have to overcome this force when aligning to the magnetic field in a different direction. The translation motions behaved as expected, with minimal undesired motion. However, as expected, there does exist some rotation about the magnetization axis, which is uncontrolled in BF mode, and is most clearly seen in the *z*-translation. The rotation about the *z*-axis is

successful, however only one rotation in either the clockwise and counterclockwise direction could be accomplished before the microrobot would reach the bottom of the work environment. This is due to the slow rotation about the magnetization axis. Higher applied torques would increase the probability of undesired behavior.

6. Conclusions

We have introduced a theoretical framework and design for six-DOF actuation of a magnetic microrobot which rely on
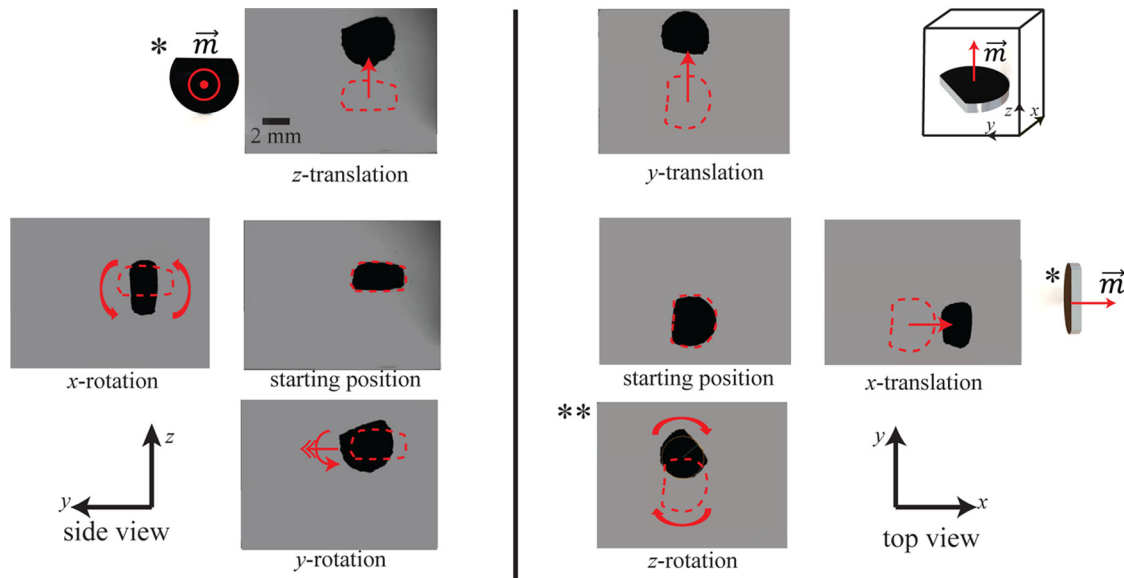
Fig. 10. Snapshots of a near-neutrally buoyant microrobot moving with six-DOF in a three-dimensional space immersed in silicone oil. Due to magnetic coil singularities, the microrobot is oriented in the *x*-direction to translate in the *z*-direction. To show that the microrobot can translate in the same direction as the magnetization direction, the microrobot is also oriented in the *x*-direction for the *x*-translation. These orientations are marked with a "*", and an alternative magnetization diagram is given. A diagram of the microrobot magnetization for the remainder of the experiments is given in the upper right-hand corner to show the microrobot's magnetization in the *z*-direction. A video of this motion is shown in Multimedia Extension 1.

a non-uniform magnetization profile within the microrobot body. As previous magnetic microrobot actuation schemes using driving systems far from the workspace cannot achieve torque about the microrobot's magnetization axis, we have shown full six-DOF magnetic actuation for the first time in such systems. In addition to the theoretical model for six-DOF actuation using permanent or non-permanent magnetic bodies, we also introduced a set of design guidelines and sufficient conditions to achieve full six-DOF control. We demonstrated the accuracy of the theoretical model through reduced-DOF water-surface experiments, demonstrating a high level of decoupling between actuation DOF. We also demonstrated full six-DOF actuation for a levitating microrobot in liquid in a proof-of-concept demonstration. Controlled translation and orientation control of a mobile microrobot with six-DOF will require feedback of microrobot orientation and implementation of a controller which can suppress the small levels of actuation error arising from imprecise microrobot fabrication and magnetization.

Acknowledgement

Conflict of interest

None declared.

Funding

Authors' note

The first three authors contributed equally to this paper.

References

Chung S, Dong X and Sitti M (2015) Three-dimensional heterogeneous assembly of coded microgels using an untethered mobile microgripper. *Lab on a Chip* 15(7): 1667–1676.

Cullity B and Graham C (2008) *Introduction to Magnetic Materials*. New York: Wiley-IEEE Press.

Diller E, Giltinan J, Lum GZ, Ye Z and Sitti M (2014a) Six-degrees-of-freedom remote actuation of magnetic microrobots. In: *Robotics science and systems*.

Diller E, Giltinan J and Sitti M (2013a) Independent control of multiple magnetic microrobots in three dimensions. *The International Journal of Robotics Research* 32(5): 614–631.

Diller E, Miyashita S and Sitti M (2012) Remotely addressable magnetic composite micropumps. *RSC Advances* 2(9): 3850–3856.

Diller E, Pawashe C, Floyd S and Sitti M (2011) Assembly and disassembly of magnetic mobile micro-robots towards deterministic 2-D reconfigurable micro-systems. *The International Journal of Robotics Research* 30(14): 1667–1680.

Diller E and Sitti M (2013) Micro-scale mobile robotics. *Foundations and Trends in Robotics* 2(3): 143–259.

Diller E and Sitti M (2014) Three-dimensional programmable assembly by untethered magnetic robotic micro-grippers, *Advanced Functional Materials* 24: 4397–4404.

Diller E, Zhang N and Sitti M (2013b) Modular micro-robotic assembly through magnetic actuation and thermal bonding. *Journal of Micro-Bio Robotics* 8(3–4): 121–131.

Diller E, Zhuang J, Zhan Lum G, Edwards MR and Sitti M (2014b) Continuously distributed magnetization profile for millimeter-scale elastomeric undulatory swimming. *Applied Physics Letters* 104(17): 174101.

Elbuken C, Khamesee M and Yavuz M (2009) Design and implementation of a micromanipulation system using a magnetically levitated MEMS robot. *IEEE/ASME Transactions on Mechatronics* 14(4): 434–445.

Frutiger DR, Vollmers K, Kratochvil BE and Nelson BJ (2009) Small, fast, and under control: wireless resonant magnetic micro-agents. *The International Journal of Robotics Research* 29(5): 613–636.

Hosokawa K, Shimoyama I and Miura H (1996) Two-dimensional micro-self-assembly using the surface tension of water. *Sensors and Actuators A: Physical* 57(2): 117–125.

Imbaby M, Jiang K and Chang I (2008) Net shape fabrication of stainless-steel micro machine components from metallic powder. *Journal of Micromechanics and Microengineering* 18(11): 115018.

Khalil IS, Magdanz V, Sanchez S, Schmidt OG and Misra S (2014) The control of self-propelled microjets inside a micro-channel with time-varying flow rates. *IEEE Transactions on Robotics* 30(1): 49–58.

Khamesee M, Kato N, Nomura Y and Nakamura T (2002) Design and control of a microrobotic system using magnetic levitation. *IEEE/ASME Transactions on Mechatronics* 7(1): 1–14.

Kim S, Qiu F, Kim S, et al. (2013) Fabrication and characterization of magnetic microrobots for three-dimensional cell culture and targeted transportation. *Advanced Materials* 25(41): 5863–5868.

Kummer M, Abbott J, Kratochvil B, Borer R, Sengul A and Nelson B (2010) OctoMag: An electromagnetic system for 5-DOF wireless micromanipulation. *IEEE Transactions on Robotics* 26(6): 1006–1017.

Mahoney AW, Cowan DL, Miller KM and Abbott JJ (2012) Control of untethered magnetically actuated tools using a rotating permanent magnet in any position. In: *IEEE international conference on robotics and automation*, pp. 3375–3380.

Martel S, Mathieu JB, Felfoul O, et al. (2007) Automatic navigation of an untethered device in the artery of a living animal using a conventional clinical magnetic resonance imaging system. *Applied Physics Letters* 90(11): 114105.

Martel S, Mohammadi M, Felfoul O, Lu Z and Pouponneau P (2009) Flagellated magnetotactic bacteria as controlled MRI-trackable propulsion and steering systems for medical nanorobots operating in the human microvasculature. *The International Journal of Robotics Research* 28(4): 571–582.

Meeker D, Maslen E, Ritter R and Creighton F (1996) Optimal realization of arbitrary forces in a magnetic stereotaxis system. *IEEE Transactions on Magnetics* 32(2): 320–328.

Miyasaka M and Berkelman P (2014) Magnetic levitation with unlimited omnidirectional rotation range. *Mechatronics* 24(3): 252–264.

Miyashita S, Diller E and Sitti M (2013) Two-dimensional magnetic micro-module reconfigurations based on inter-modular interactions. *The International Journal of Robotics Research* 32(5): 591–613.

Pawashe C, Floyd S, Diller E and Sitti M (2012) Two-dimensional autonomous microparticle manipulation strategies for magnetic microrobots in fluidic environments. *IEEE Transactions on Robotics* 28(2): 467–477.

Pawashe C, Floyd S and Sitti M (2009) Modeling and experimental characterization of an untethered magnetic micro-robot. *International Journal of Robotics Research* 28(8): 1077–1094.

Sakar MS, Steager EB and Kim DH (2011) Modeling, control and experimental characterization of microbiorobots. *The International Journal of Robotics Research* 30(6): 647–658.

Tasoglu S, Diller E, Guven S, Sitti M and Demirci U (2014) Untethered micro-robotic coding of three-dimensional material composition. *Nature Communications* 5(3124).

Tottori S, Zhang L, Qiu F, Krawczyk KK, Franco-Obregón A and Nelson BJ (2012) Magnetic helical micromachines: fabrication, controlled swimming, and cargo transport. *Advanced Materials* 24(6): 811–816.

Vartholomeos P, Akhavan-sharif MR and Dupont PE (2012) Motion planning for multiple millimeter-scale magnetic capsules in a fluid environment. In: *IEEE international conference on robotics and automation*, pp. 1927–1932.

Vartholomeos P, Bergeles C, Qin L and Dupont PE (2013) An MRI-powered and controlled actuator technology for tetherless robotic interventions. *The International Journal of Robotics Research* 32(13): 1536–1552.

Ye Z, Diller E and Sitti M (2012) Micro-manipulation using rotational fluid flows induced by remote magnetic micro-manipulators. *Journal of Applied Physics* 112(6): 064912.

Ye Z and Sitti M (2014) Dynamic trapping and two-dimensional transport of swimming microorganisms using a rotating magnetic micro-robot. *Lab on a Chip* 14(13): 2177–2182.

Appendix: Index to Multimedia Extension

Archives of IJRR multimedia extensions published prior to 2014 can be found at http://www.ijrr.org, after 2014 all videos are available on the IJRR YouTube channel at http://www.youtube.com/user/ijrrmultimedia

Table of Multimedia Extension

Extension	Media type	Description
1	Video	Experimental demonstrations of water surface and submerged six-DOF actuation of a discrete-magnet microrobot prototype, corresponding to Figures 9 and 10.